Supporting information

Contamination in dielectric barrier discharge plasmas by electrode erosion

Robin De Meyer[1, 2, 3], Jo Verbeeck[2], Sara Bals[2, 3,*] and Annemie Bogaerts[1,*]

[1] *Research group PLASMANT, Department of Chemistry, University of Antwerp, Universiteitsplein 1, 2610 Antwerp, Belgium*
[2] *Research group EMAT, Department of Physics, University of Antwerp, Groenenborgerlaan 171, 2020 Antwerp, Belgium*
[3] *Nanolab Centre of Excellence, University of Antwerp, Groenenborgerlaan 171, 2020 Antwerp, Belgium*

* corresponding author: annemie.bogaerts@uantwerpen.be
* corresponding author: sara.bals@uantwerpen.be

Contents

S1. Experimental Methods

S1.1. DBD reactor schematic and technical details

The experimental setup is schematically presented in Figure S1, including the precise dimensions of the reactor. The gases (Air Liquide; Ar ≥ 99.999 %, He ≥ 99.999 %, CO_2 ≥ 99.998 %) were controlled by a mass flow controller (Bronkhorst). The plasma was generated using the G10 S-V AFS GmbH power supply unit (PSU) set at 23.5 kHz, while the discharge was monitored using a high voltage probe (Tektronix P6015A), a current monitor (Pearson Electronics 4100, high-frequency 3 dB point approx. 35 MHz), and a low voltage probe (Pico Technology TA150) across a 10 nF monitoring capacitor. All probes were connected to a Picoscope 6402A (Pico Technology, bandwidth 250 MHz) oscilloscope that was used to save snapshots of the discharge for later analysis. The inner electrode of the reactor is made of 304 stainless steel, while the dielectric barrier consists of alumina (Al_2O_3). The reactor was packed with pristine γ-Al_2O_3 spheres (Sasol) with a diameter of 1.8 mm prior to each experiment. This setup was previously described and characterized in detail in [1].

The gas flow rate was set at 100 mls/min with a constant applied power, yielding a relatively stable plasma power of 45-50 W for Ar and He, and around 60-65 W for the CO_2 discharge, as presented in Section S4.
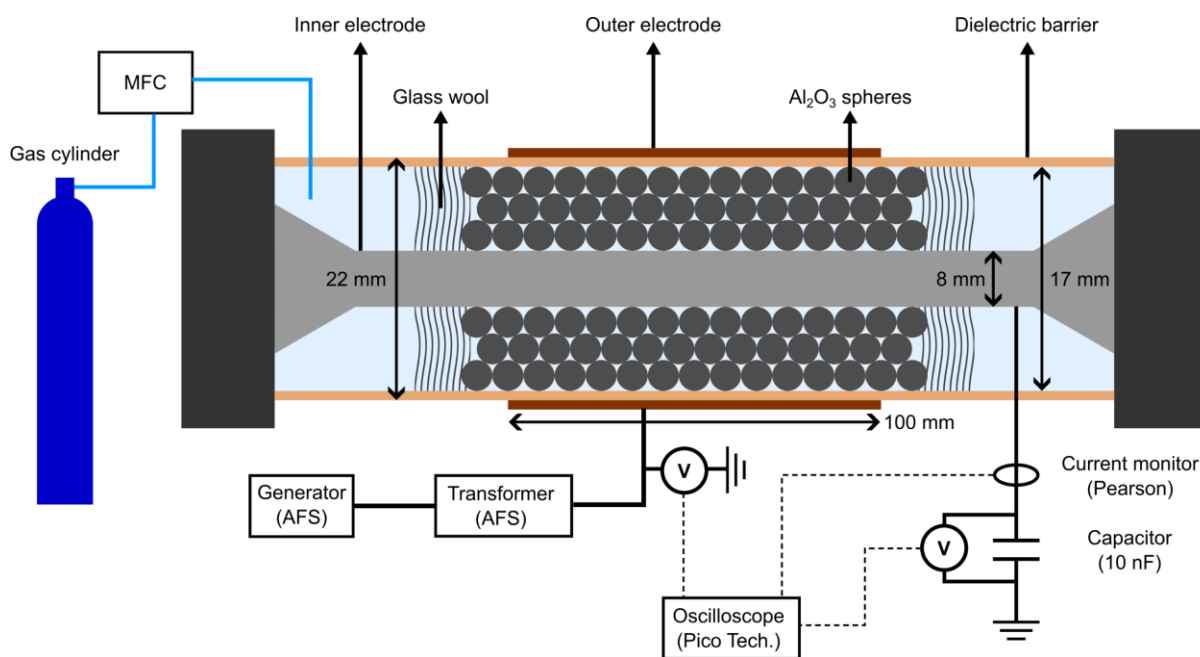

Figure S1: Schematic of the complete experimental setup including reaction dimensions. This figure is an adapted version of a figure that was previously published in[1].

S1.2. SEM and TEM parameters

S1.2.1. SEM

For the SEM analyses, a Thermo Fisher Scientific Quanta 250 ESEM was employed. An acceleration voltage of 20 kV was used, with a working distance of 10 mm, while operating the microscope in its high vacuum mode. The built-in Everhart-Thornley (secondary electron, SE) detector, as well as the pole piece-mounted backscattered electron (BSE) detector were used. An Oxford Instruments energy dispersive and wave dispersive X-ray detector were used to identify three key elements in the particles of interest: Fe, Cr, Ni. Both detectors were used at some point, depending on technical operability of the detectors at the time of the various analyses.

Prior to the analyses, entire spheres were attached to a SEM stub using silver paint, after which the exposed surfaces of the spheres were coated with approximately 25 nm of carbon to improve surface conductivity.

S1.2.2. TEM

The TEM analyses were performed using a Thermo Fisher Scientific Tecnai Osiris microscope operated at 200 kV, with a camera length of 115 mm. HAADF-STEM imaging and EDX-STEM analyses were performed to identify and investigate the stainless steel particles. A beam current of approximately 125 pA was used. Prior to the TEM analyses, 5 spheres were added to a vial with approximately 1 ml of acetone, after which the sample was vortexed and sonicated for around 30 seconds each. Next, a few drops of the resulting liquid were dropcast on a holey carbon TEM support grid, which was left to dry in ambient conditions.

For the bright field TEM analysis of the steel particles in a carbon matrix (Figure S9 C below), the same microscope was used, operated at 200 kV in conventional brightfield TEM imaging mode. A small amount of the material formed in the reactor was added to a vial and sonicated together with a few drops of acetone. Then, a few drops of this suspension were dropcast on a holey carbon grid, prior to TEM analysis.

S1.2.3. A note on bias

For the SEM analyses, the spheres were manipulated minimally, ensuring a maximally representative sample in the SEM. However, the experimental conditions were challenging. Indeed, stainless steel particles, usually just hundreds of nm large, were scattered across an Al_2O_3 sphere of almost 2 mm in diameter. In addition, the concentration of particles was low. This meant that large areas of the sphere had to be searched for few and small particles. Due to the presence of impurities in the pristine Al_2O_3 spheres, automating this process proved challenging. Therefore, it is likely that the actual data acquired is somewhat biased, most likely towards larger particles, as they would stand out more against the lighter background. Furthermore, the SEM may also have been resolution-limited, especially when screening areas at a relatively low magnification, possibly further biasing the data. However, as all samples were treated and analyzed in the same way, we believe relative comparisons between the samples are still highly relevant. For the TEM analyses, a similar bias towards larger particles may be expected. However, in addition, the samples were manipulated quite drastically in order to be able to analyze the stainless steel particles themselves. It is plausible that in this process, a sort of pre-selection of stainless steel particles was made, as some particles may have stronger or weaker interactions with the support than others, thus potentially introducing another bias to the analyses. However, again, since all samples were manipulated and analyzed using an identical approach, a relative comparison should still be valid. Though, due to the differences in sample manipulation, a direct comparison between SEM and TEM data may be less justified.

S2. Representative EDX spectra

S2.1. SEM-EDX

A representative SEM-EDX spectrum is presented in Figure S2. The spectrum shows strong O and Al signals, which makes sense given that the particle was on an Al_2O_3 sphere during analysis. Indeed, when employing SEM-EDX for such relatively small particles, the primary electron beam interacts with a larger volume than just the particle of interest in this case, yielding the strong O and Al signals. However, when highlighting the relevant energy range, clear signals for Fe, Cr, Ni, and even Mn were also observed, thus confirming the composition of the stainless steel particle.
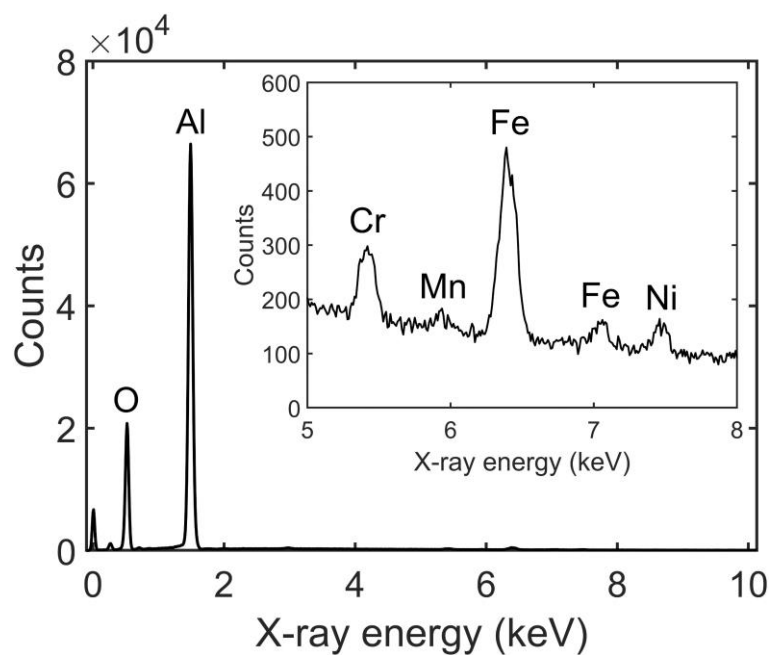

Figure S2: Representative SEM-EDX spectrum from a stainless steel particle on the surface of an Al_2O_3 sphere, used in the Ar plasma. Strong Al and O peaks are present due to the Al_2O_3 support, while Fe, Cr, and Ni could be observed, confirming the composition of the stainless steel particle.

S2.2. TEM-EDX

In Figure S3, a representative EDX spectrum as obtained in the TEM is presented. The composition of the particles can again be confirmed by identifying the Fe, Cr, Ni, and Mn signals, clearly indicating that the particle is stainless steel. In addition to these elements, Al and O were again observed as they make up the Al_2O_3 support material that was still present during TEM analysis, though the peaks are not as dominant due to the different geometry compared to the SEM. Finally, also Cu and C signals were observed, but these can be attributed to the support on which the sample was deposited for TEM analysis.
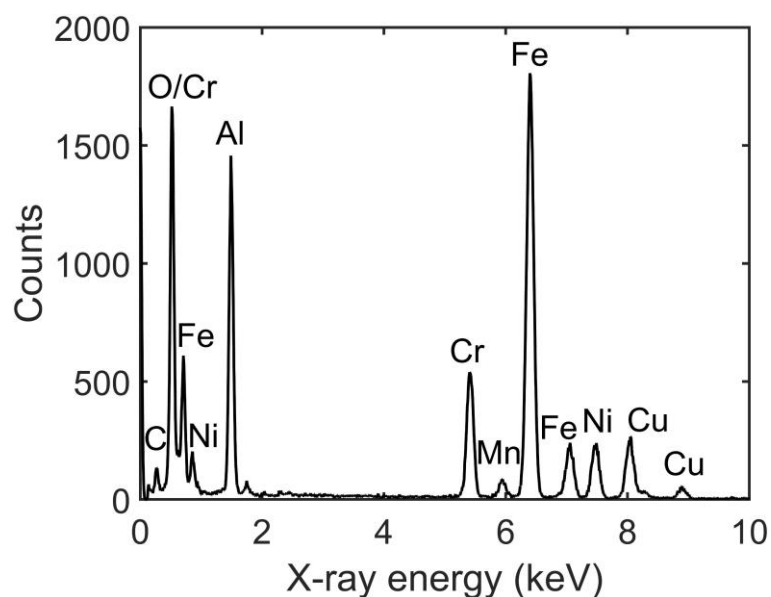

Figure S3: Representative TEM-EDX spectrum for a stainless steel particle, extracted from an Al_2O_3 sphere that was exposed to the CO_2 plasma. The identifying elements for stainless steel (Fe, Cr, Ni) are clearly present. In addition, Cu and C signals were also observed, but these can be attributed to the TEM support on which the sample was deposited.

S3.   Particle size distribution fits

The histograms presenting the measured particle sizes are shown in Figure 3 of the main text, as well as lognormal fits of these data. A Lilliefors test for normality was performed on the logarithms of the particle sizes of each sample. For every dataset, the Lilliefors test accepted the null hypothesis that the data comes from a normal distribution, justifying the lognormal fit. Furthermore, two-sample t-tests revealed significant differences between the different sets of logarithmic values, proving that there is a significant difference between the various particle size distributions.

S4. Plasma power over time

The plasma power was determined at every timestep (average of three snapshots), and is presented in Figure S4. After the initial thermal stabilization, the plasma power remains quite stable over time, though a slight decreasing trend may be observed for the CO_2 plasma. Despite being operated at the same "PSU power", i.e., the power set on the power supply (100 W), the actual plasma powers differ significantly. The plasma power for the Ar and He discharge are (after thermal stabilization) 45-50 W, while the plasma power for the CO_2 discharge is 60-65 W.
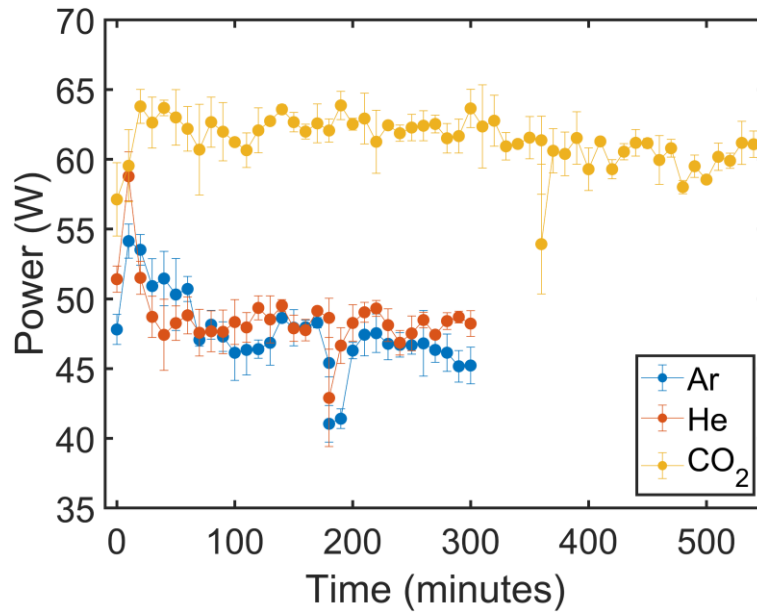

Figure S4: Plasma power over time for all gases.

S5. Discharge characteristics and thermal effect

The discharging areal fraction β and microdischarge quantity over time are presented below, for the Ar (Figure S5), He (Figure S6), and CO_2 (Figure S7) discharge. Note that the y-axes are different to reveal the details of the data, while major difference may be present between the different gases. The orange data points indicate the second phase of each experiment, so after reignition once cooled down to room temperature. In most cases, the first half hour shows some additional variation of the values due to heating of the system, but after that, the trend from the end of the first phase continues. Only the discharging areal fraction during the CO_2 discharge appears to reach the previous value slightly slower, but is still very near those values. These results indicate that, especially for the Ar and He discharges, there is a cumulative effect independent of the temperature, i.e., something is changing in the system, that is causing the plasma discharge characteristics to vary slightly.
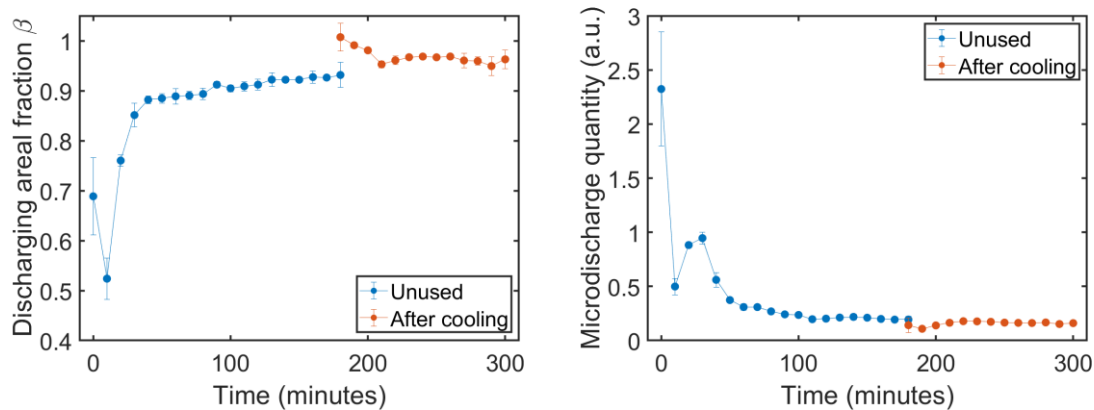

Figure S5: Discharging areal fraction β (left) and microdischarge quantity (right) during the Ar discharge. The orange data points indicate the data after cooling down. The increasing trend of the discharging areal fraction continues after thermal stabilization upon reigniting the plasma, and the same goes for the decreasing trend of the microdischarge quantity.
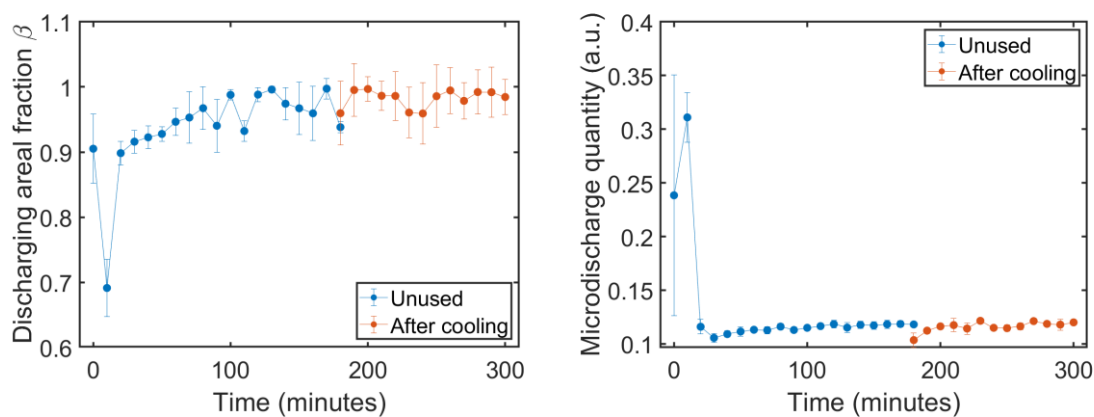

Figure S6: Discharging areal fraction β (left) and microdischarge quantity (right) during the He discharge. The orange data points indicate the data after cooling down. The large variations after the initial ignition are not observed upon reigniting the plasma after cooling down.
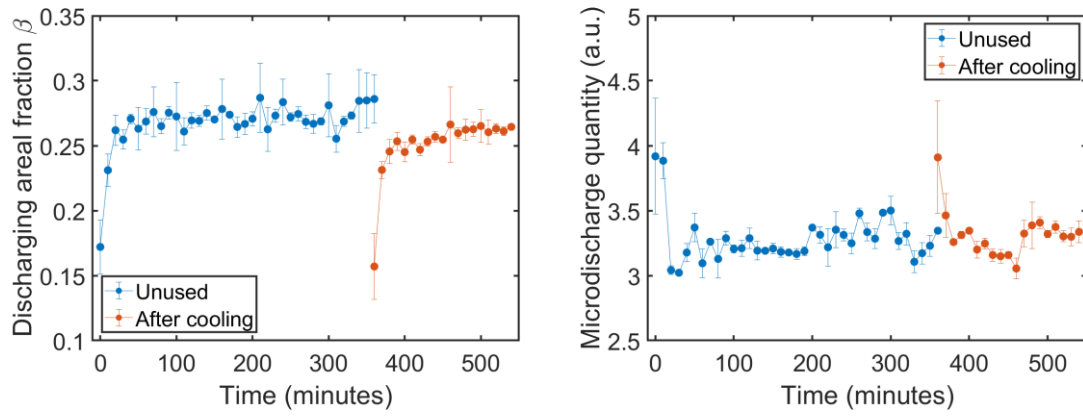
9

Figure S7: Discharging areal fraction β (left) and microdischarge quantity (right) during the CO_2 discharge. The orange data points indicate the data after cooling down. No clear cumulative effect is observed, and similar behavior can be found after reignition compared to the initial ignition.

S6. Samples used in other DBD reactors

Two additional spent packing materials that were used in completely different packed-bed DBDs and operated under different conditions were kindly provided for additional analyses. These samples were analyzed by SEM and energy dispersive X-ray spectroscopy (EDX) to investigate whether they also contained stainless steel particles. While both additional samples were used in distinctly different reactors, they all have an exposed stainless steel central electrode in common. Our analyses revealed that both additional samples also contained stainless steel particles, and examples are presented in Figure S8. Their composition was again confirmed by EDX. The technical specifications of the reactors used are provided in Table S1. It is clear that they span a wide range of properties, highlighting that this phenomenon is not unique to a particular system.
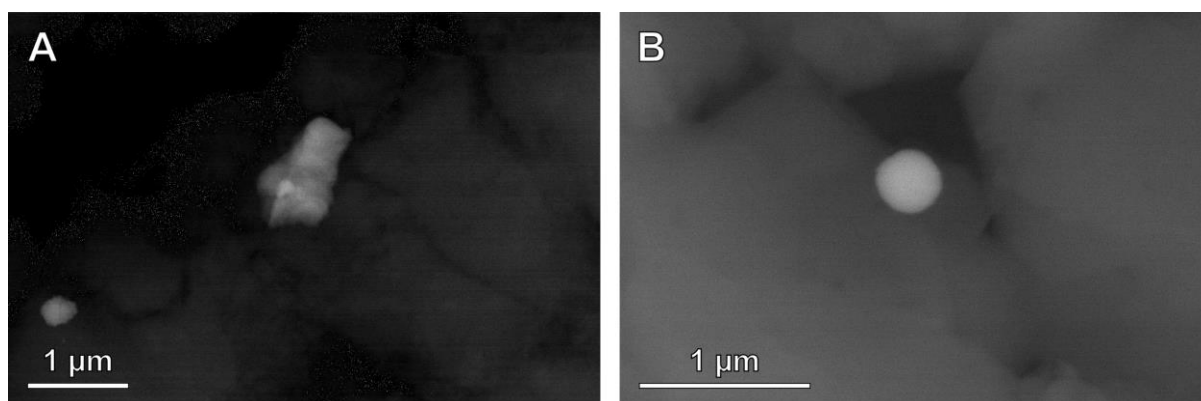

Figure S8: BSE-SEM images of stainless steel particles found on a silica (A) and zeolite 5A (B) support after being used in a packed-bed DBD experiment.

Table S1: Specifications of the packed-bed DBD reactors in which the presented samples were used.

Packing material	alumina (this work)	silica	zeolite 5A[2]
Discharge gap (mm)	4.5	2.5	1
PSU frequency (kHz)	23.5	23.5	45
Plasma power (W)	45-65	ca. 25	ca. 30
Dielectric material	alumina	glass (water cooled)	alumina
Inner electrode material	stainless steel	stainless steel	stainless steel
Discharge gas	Ar, He, or CO_2	$CO_2 + H_2$	$CO_2 + CH_4 + Ar$

S7. Steel particles in carbon matrix formed in CH$_4$ plasma

The same reactor that was used for the silica sample from Section S6 was used empty to generate a pure CH$_4$ plasma. After operating the plasma continuously for 2 h with a plasma power of ca. 25 W, carbon deposits were collected and analyzed. The SEM and TEM data are presented in Figure S9. All data clearly illustrate the presence of steel particles on and throughout the carbon material. The brightfield TEM analyses even revealed very small particles, down to 2-3 nm. The representative SEM-EDX spectrum again confirms that the particles are indeed stainless steel.
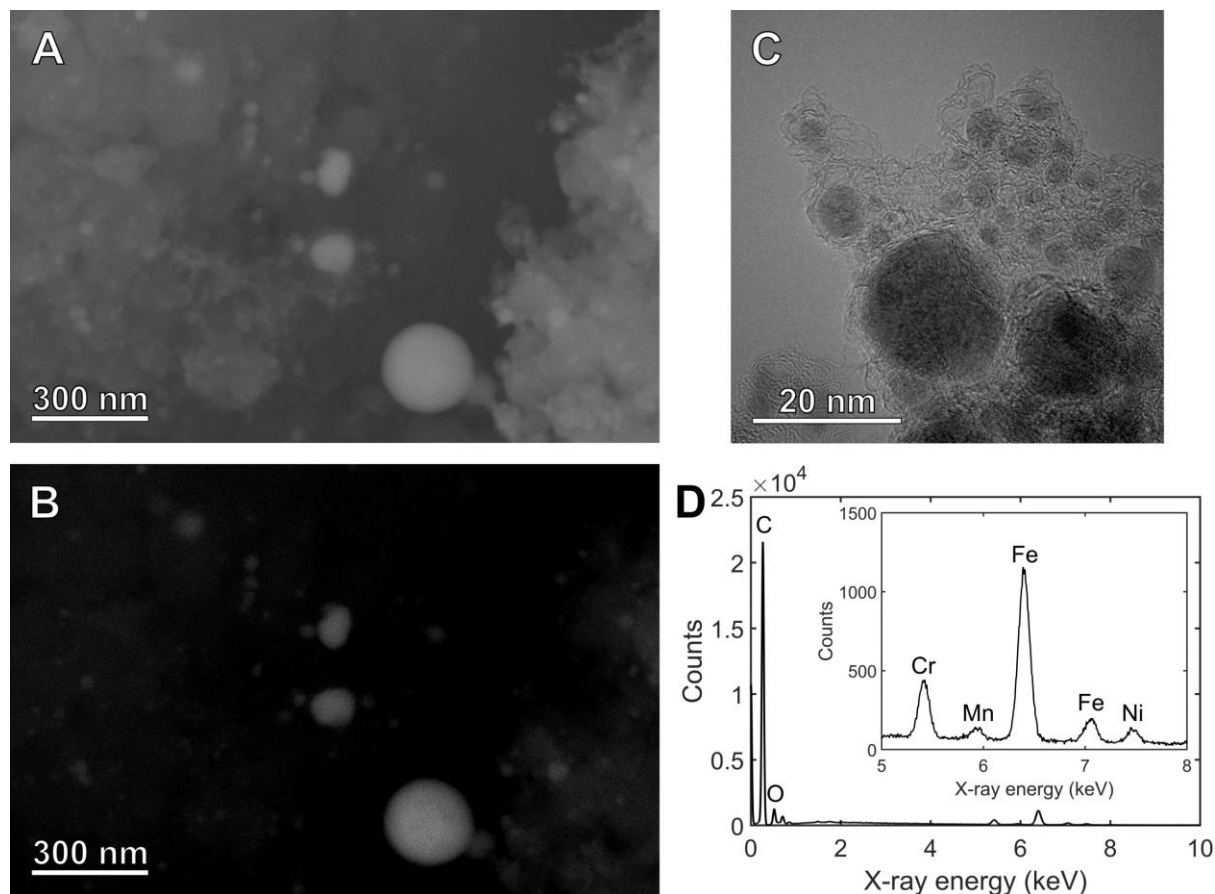

Figure S9: A, B: SE- (A) and BSE- (B) SEM images of the carbon deposits that were generated in the empty DBD with a CH$_4$ plasma. Heavy (steel) particles are clearly present in the carbon material. C: Brightfield TEM image of steel nanoparticles inside the carbon material. D: Representative SEM-EDX spectrum of the heavy particles in the carbon material, clearly containing Fe, Cr, and Ni, identifying the particles as stainless steel.

S8. References

(1) De Meyer, R.; Gorbanev, Y.; Ciocarlan, R.-G.; Cool, P.; Bals, S.; Bogaerts, A. Importance of Plasma Discharge Characteristics in Plasma Catalysis: Dry Reforming of Methane vs. Ammonia Synthesis. *Chemical Engineering Journal* **2024**, *488*, 150838. https://doi.org/10.1016/j.cej.2024.150838.

(2) Vertongen, R.; De Felice, G.; Van Den Bogaard, H.; Gallucci, F.; Bogaerts, A.; Li, S. Sorption-Enhanced Dry Reforming of Methane in a DBD Plasma Reactor for Single-Stage Carbon Capture and Utilization. *ACS Sustainable Chem. Eng.* **2024**, *12*, 10841–10853. https://doi.org/10.1021/acssuschemeng.4c02502.